

Near-adiabatic quench experiments on short $\text{YBa}_2\text{Cu}_3\text{O}_{7-\delta}$ coated conductors

X. Wang

*Center for Advanced Power Systems, Florida State University, Tallahassee, Florida 32310;
Department of Electrical and Computer Engineering, Florida State University, Tallahassee, Florida 32310;
and National High Magnetic Field Laboratory, Florida State University, Tallahassee, Florida 32310*

U. P. Trociewitz

National High Magnetic Field Laboratory, Florida State University, Tallahassee, Florida 32310

J. Schwartz^{a)}

*Center for Advanced Power Systems, Florida State University, Tallahassee, Florida 32310;
Department of Mechanical Engineering, Florida State University, Tallahassee, Florida 32310;
and National High Magnetic Field Laboratory, Florida State University, Tallahassee, Florida 32310*

(Received 16 October 2006; accepted 11 December 2006; published online 6 March 2007)

Minimum quench energy and normal zone propagation velocity are measured on short $\text{YBa}_2\text{Cu}_3\text{O}_{7-\delta}$ coated conductors in self-field at temperatures ranging from 40 to 77 K. The sample is cooled via a cryocooler with a cryostat pressure of $\sim 10^{-4}$ Pa, creating a nearly adiabatic environment. A normal zone is created by pulsing a heater that is attached to the sample surface with a thin layer of alumina-filled epoxy. The minimum quench energy is determined by identifying the minimum heater energy that creates a propagating normal zone, and the propagation velocity is determined from the time delay between voltage signals in voltage taps distributed along the length of the conductor. It is found that the minimum quench energy is on the order of 1 J and the normal zone propagation velocity ranges from 1–40 mm/s. These results are compared to similar measurements on other coated conductor architectures and geometries and to the classical adiabatic quench propagation model. © 2007 American Institute of Physics. [DOI: [10.1063/1.2435804](https://doi.org/10.1063/1.2435804)]

I. INTRODUCTION

The adiabatic operation of high- T_c superconducting magnets is envisioned because they have a large energy margin for stable operation. On the other hand, high- T_c magnets are not likely to be self-protecting due to their low normal zone propagation velocity and thus active protection techniques are required.^{1–4} Of the potential technical high- T_c superconductors, $\text{YBa}_2\text{Cu}_3\text{O}_{7-\delta}$ (YBCO) coated conductors are promising candidates for dc and ac applications.⁵ These conductors have high critical current density over a broad range of temperature and magnetic field, surpassed in electrical performance only at 4.2 K, where isotropic conductors (Nb_3Sn and $\text{Bi}_2\text{Sr}_2\text{CaCu}_2\text{O}_x$) are preferred.

One of the engineering issues that must be addressed before YBCO coated conductors can be used in large magnets is quench protection. Before magnet protection can be addressed, however, the quench behavior of conductors must be understood. There are a few reports in the literature of such behavior. In these reports, samples were conduction cooled either at one fixed temperature^{6–8} or at different ambient temperatures.^{9–11} Experiments on samples cooled by nitrogen gas, boiling liquid nitrogen, and forced flow nitrogen^{12–16} have been reported, as have experiments in a 5 T background magnetic field.¹⁰ Current sharing in striated YBCO coated conductors, developed primarily for ac applications, is discussed in Ref. 17. Most recently, the relation-

ship between quenching, mechanical behavior, and conductor failure has been reported.¹⁸ These experiments show a normal zone propagation velocity on the order of 10^{-3} – 10^{-2} m/s,^{8,11,12} which is two to three orders of magnitude slower than the velocity for low- T_c magnets operating at 4.2 K.^{19,20} Thus, one of the primary challenges for protecting high-temperature superconducting magnets will be quench detection. To develop effective quench detection and protection schemes, a thorough understanding of the minimum quench energy and the normal zone propagation velocity is essential.

In this paper, the minimum quench energy and normal zone propagation velocity of YBCO coated conductors is reported. In these experiments, the conductor is cooled via a cryocooler in a nearly adiabatic environment. Results are compared to those of the classical adiabatic model and to previous measurements on different YBCO architectures and geometries.

II. EXPERIMENTAL APPROACH

A. YBCO coated conductor sample

A 4 mm wide, 180 mm long coated conductor sample, “SPI,” was provided by IGC SuperPower, Incorporated. The sample was received in January 2005 and is typical of samples of that time frame. The sample was fabricated by ion-beam-assisted deposition on a Hastelloy C276 substrate. The architecture is shown in Fig. 1; a 100 μm thick Hastelloy substrate is coated with a 1 μm thick buffer layer, a

^{a)}Author to whom correspondence should be addressed; electronic mail: schwartz@magnet.fsu.edu

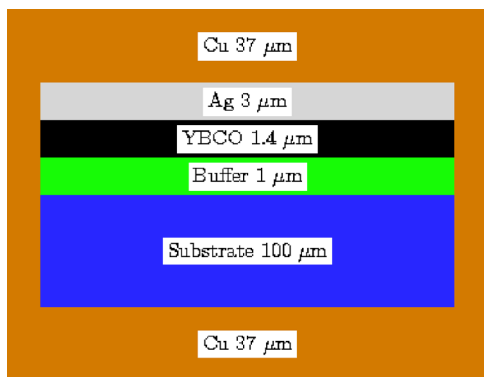


FIG. 1. (Color online) Schematic cross section of the YBCO coated conductor architecture (layer thicknesses are shown; drawing not to scale).

1.4 μm thick YBCO layer, and a 3 μm thick Ag layer. The conductor is stabilized by electroplating a 37 μm thick layer of Cu on both sides. More details on the sample preparation process are found in Ref. 21.

B. Instrumentation

A schematic showing the voltage taps and thermocouples, mounted on the sample surface (YBCO-facing side), is seen in Fig. 2. The Cu wire (0.160 mm diameter) voltage taps are soldered with 10 mm spacing. These are used to monitor the time-varying voltages as a function of location along the tape, $V(x,t)$, during quench experiments. Thermocouple junctions, made by spot-welding the ends of type- E thermocouple wire (0.127 mm diameter) pairs, are attached between the voltage taps using GE varnish. The other ends of the thermocouple wire pairs are spot welded with Cu extensions and submerged in liquid nitrogen. These provide the thermal reference point.

All the instruments are connected via an IEEE-488 GPIB bus and controlled by a PC running LABVIEW. The instruments are triggered by a bus trigger to ensure signal synchronization. The voltage differences between the voltage taps are measured by an array of parallel-connected digital multimeters (DMMs) and a digital storage oscilloscope. The data acquisition rate for the oscilloscope is 16 ms/data point. The DMM array consists of buffered and unbuffered DMMs. For the buffered DMMs, the data acquisition rate is 14 ms/data point. The unbuffered DMMs transfer one data point to the PC controller sequentially and do not take the next data point until all unbuffered DMMs have completed the data transfer. Thus, the unbuffered DMMs make voltage measurements simultaneously and have an effective data acquisition rate of

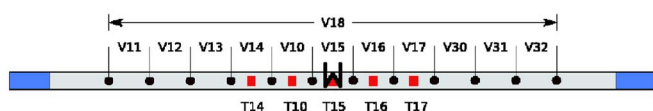


FIG. 2. (Color online) Schematic diagram of voltage taps and thermocouples along the sample for quench experiments (not to scale). Solid circles represent solder dots where voltage taps are connected. These are 10 mm apart. Solid squares represent thermocouple junctions. The W-shaped heater is also shown. Solid rectangles at the sample ends represent low temperature solders for connecting the sample to the current leads; each is 20 mm long.

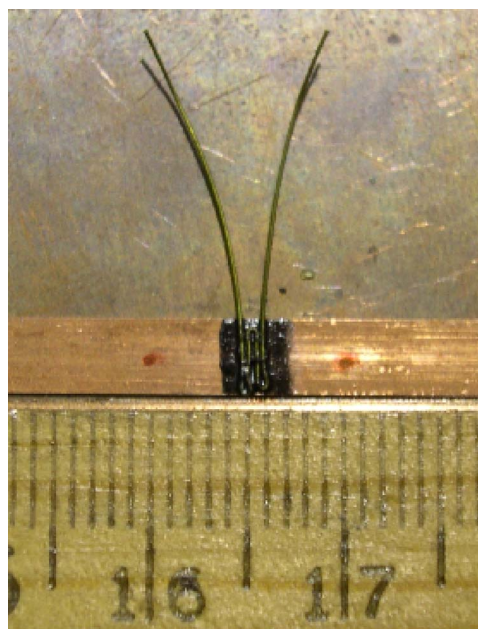


FIG. 3. (Color online) The W-shaped heater attached to the sample surface before it is covered by epoxy.

~ 43 ms/data point. The thermocouple voltages are scanned by a scanner card within a DMM which buffers the data. Each temperature measurement requires ~ 30 ms (channel switching and voltage measurement), so since ten channels are scanned per cycle, the effective temporal resolution for temperature measurements is ~ 0.3 s/channel.

A W-shaped 80% Ni–20% Cr wire (0.203 mm diameter, 1.5 mm “tip to tip” along the conductor) is attached to the sample surface (YBCO-facing side) using alumina-filled epoxy (see Fig. 3). The heater is located in section V_{15} , which is the center of the sample. A small heater is desired in order to emulate a localized disturbance; if the heater is too small, however, then it is not possible to introduce enough heat to quench the conductor. A thermocouple is attached atop the heater. A sketch of the heater, epoxy, and thermocouple is shown in Fig. 4.

The sample is wound around a thin-wall cylindrical Cu sample holder (80 mm diameter). A thin layer of tissue is sandwiched between the sample and the sample holder to prevent contact; a gap is maintained between the sample and the tissue. A mounted sample with voltage taps, thermocouples, and the heater is seen in Fig. 5. The sample holder is thermally anchored to the second stage of a GM cryocooler

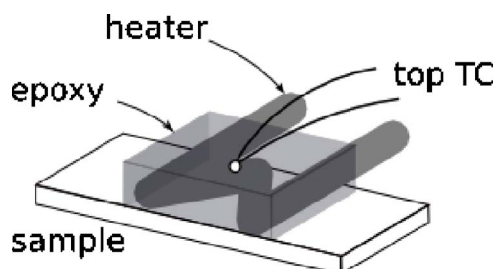


FIG. 4. (Color online) Idealized schematic drawing of the heater, epoxy, thermocouple, and sample for the quench experiments. The thermocouple (TC) junction is attached atop the epoxy.

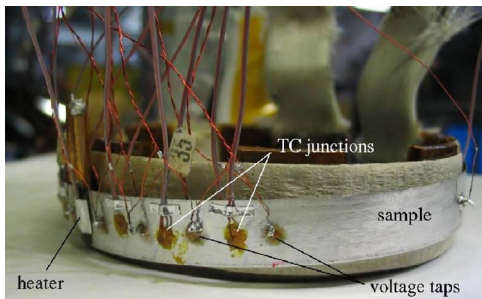


FIG. 5. (Color online) A YBCO sample mounted on the sample holder. Also seen are voltage taps, thermocouples, and the heater.

which provides 2.25 W of cooling at 20 K. A pair of superconducting current leads, each made of five Ag-alloy sheathed $(\text{Bi,Pb})_2\text{Sr}_2\text{Ca}_2\text{Cu}_3\text{O}_x$ tapes and backed with Cu, is used to transport the current to the sample. The current leads are thermally anchored at the first and second stages of the cryocooler. The sample ends are soldered to the current leads. Several layers of aluminized Mylar superinsulation foil are wound around the probe to reduce thermal radiation. More details are given in Refs. 11 and 12.

C. Experimental protocol

The entire experimental assembly (cold head, sample holder, and sample) hangs within a cryostat which is pumped down to a pressure of $\sim 10^{-4}$ Pa. The quench experiments are run in a quasiadiabatic environment. Sample cooling is achieved primarily through the current leads. A stable operating temperature along the sample, ranging from 40 to 77 K, is controlled by a temperature controller that powers a Kapton-insulated thin-film heater attached to the bottom surface of the sample holder. A Cernox sensor is attached to the top of the heater to provide feedback to the proportional-integral-derivative (PID) control loop. The PID coefficients are tuned automatically by the temperature controller. When the sample temperature increases during a quench, the Cernox temperature also increases slightly but stabilizes to the set temperature within 3 min.

Quench experiments begin by establishing the desired temperature in the sample. The critical current (I_c) as a function of location along the conductor is then measured using the array of voltage taps and a $1 \mu\text{V}/\text{cm}$ electric field criterion. The transport current (I_t) is then ramped to the desired fraction of the end-to-end I_c using a fixed ramp rate controlled by a ramp generator. In all experiments, the initial I_t is less than the local minimum I_c in the conductor, ensuring that a stable equilibrium can be obtained. Once a stable equilibrium at the desired I_t and T is established, the heater is pulsed (300 ms) to induce a local thermal disturbance in the conductor, and the conductor voltages and temperatures as functions of time and location are monitored. Initially, the heat pulse amplitude is low. If the conductor is not quenched, the sample is recooled to the desired temperature and the experiment is repeated with a higher heater pulse amplitude. This procedure is repeated until the conductor voltages increase without recovery, indicating that the conductor is quenched. At this point, the experiment is discontinued to

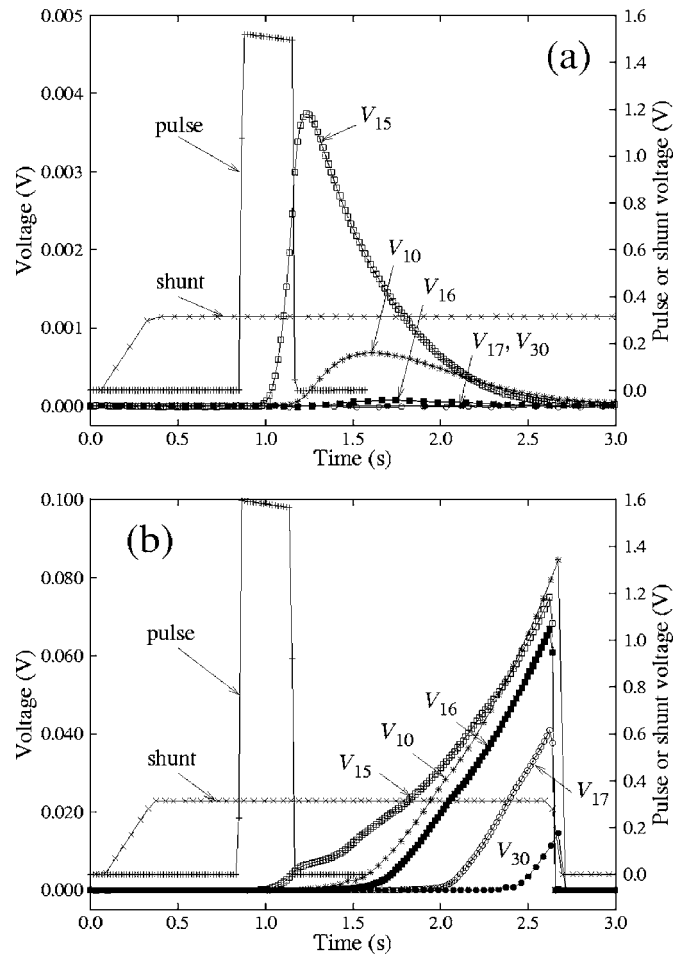


FIG. 6. $V(t)$ data measured at 40 K, $I_t/I_c=0.70$. (a) A 1.51 V heater pulse amplitude, corresponding to a heat input of 0.86 J, did not result in a quench, while (b) a heater 1.59 V heater pulse height, corresponding to a heat input of 0.97 J, resulted in a quench. Note that there is a factor of 20 difference in the voltage ranges.

protect the sample from damage by quickly zeroing the transport current. The minimum quench energy (MQE) is defined as the minimum heater energy required to quench the conductor. Figure 6 shows a typical transient $V(t)$ (a) for a stable recovery (no quench) and (b) for a quench at 40 K. Also plotted are the voltage across a shunt that is in series with the transport current (“shunt”) and the heater voltage (“pulse”). Note that the scale on the primary y axis in 6(b) is 20 times that of 6(a). The corresponding $T(t)$ data are shown in Fig. 7. After determining the MQE at one I_t/I_c , the procedure is repeated at the same temperature for a lower I_t/I_c value. In this manner, MQE vs I_t/I_c is measured for $I_t/I_c = 0.90$ to 0.30 in steps of 0.20. Another temperature is then selected and the entire procedure repeated for $T=40, 50, 60, 70,$ and 77 K.

III. RESULTS AND DISCUSSION

A. Critical current versus temperature

The end-to-end $I_c(T)$ is shown in Fig. 8(a) and $I_c(T)$ versus location along the sample is shown in Fig. 8(b) (the end-to-end I_c is in section V_{18}). Also plotted in Fig. 8(a) are

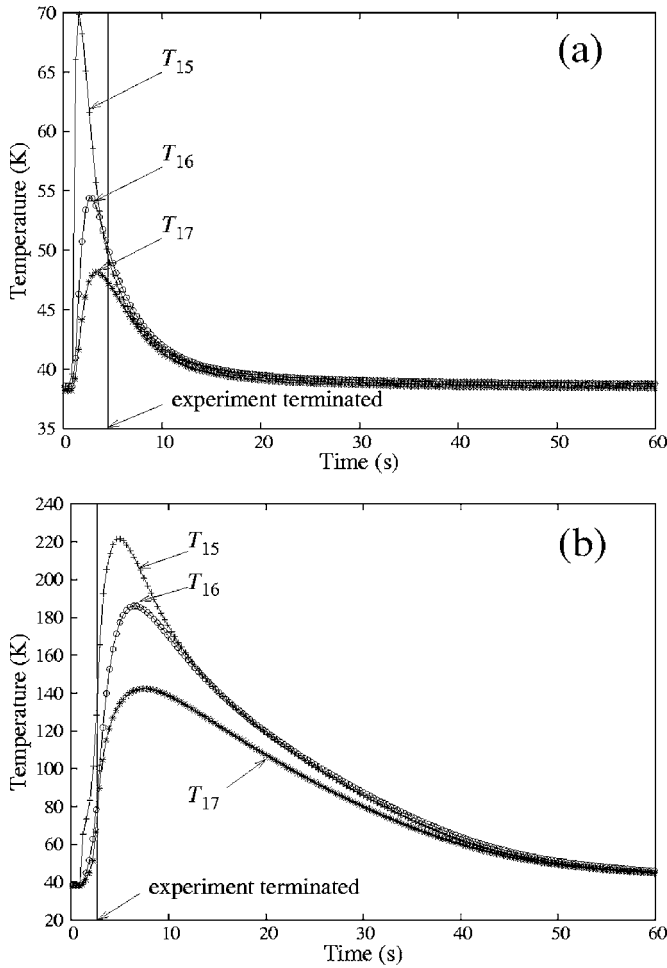


FIG. 7. $T(t)$ data measured at 40 K, $I/I_c=0.70$, corresponding to the $V(t)$ data in Fig. 6

the standard deviations, determined by averaging the data in Fig. 8(b). The standard deviations and the curves in Fig. 8(b) illustrate the sample homogeneity.

The sample experienced 164 heater pulses (quench attempts) to determine the MQE and normal zone propagation velocity (NZPV) at 40, 50, 60, 70, and 77 K. In these experiments, the sample was quenched 77 times and recovered 87 times. No changes in I_c were found after the series of experiments. The maximum local temperature measured in any experiment was 250 K.

B. Minimum quench energy

To accurately determine the MQE when using a pulsed heater to initiate quenching, it is necessary to consider the heat absorbed by the epoxy used to attach the heater, the heat removed by the surrounding atmosphere, and the heat conduction to the current leads.²⁰ In these experiments, the surrounding pressure is very low and the conditions are nearly adiabatic with respect to surface cooling. Cooling at the sample ends is also neglected because, as seen in Fig. 6, the voltage and temperature propagation is sufficiently slow that the central section of the conductor either has recovered or is quenched and the experiment discontinued before the ends of

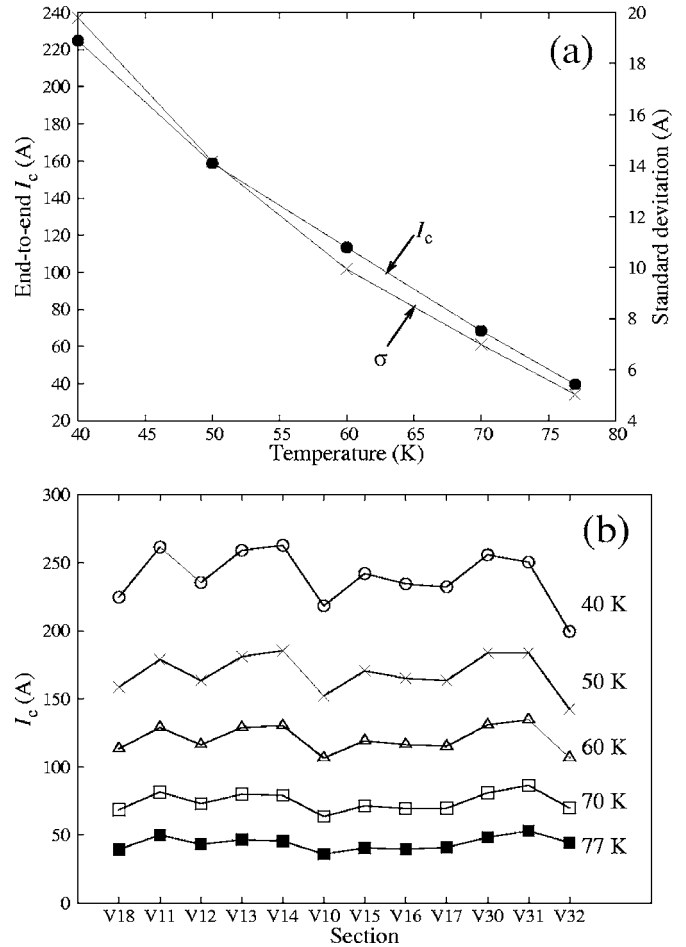


FIG. 8. (a) End-to-end $I_c(T)$ and (b) $I_c(T)$ vs location along the sample. Also plotted in (a) are the standard deviations, determined by averaging the data in (b).

the sample show any voltage increase. Thus, only the energy absorbed by the epoxy must be factored and the MQE becomes

$$MQE = E_{hr} - E_{epo}, \tag{1}$$

where E_{hr} is the heat generated in the heater and E_{epo} the energy absorbed by the epoxy. Given the minimum heat pulse voltage that quenches the sample, $V_{min}(t)$, the heater resistance $R(t)$, and the heat pulse duration $t_p=300$ ms, E_{hr} becomes

$$E_{hr} = \int_0^{t_p} \frac{V_{min}^2(t)}{R(t)} dt. \tag{2}$$

$V_{min}(t)$ is measured and is nearly constant, so assuming that $R(t)$ is not strongly temperature dependent during the 300 ms heat pulse, Eq. (2) is simplified to

$$E_{hr} = \frac{V_{min}^2}{R} t_p, \tag{3}$$

where V_{min} and R are constant. The energy absorbed by the epoxy is estimated using

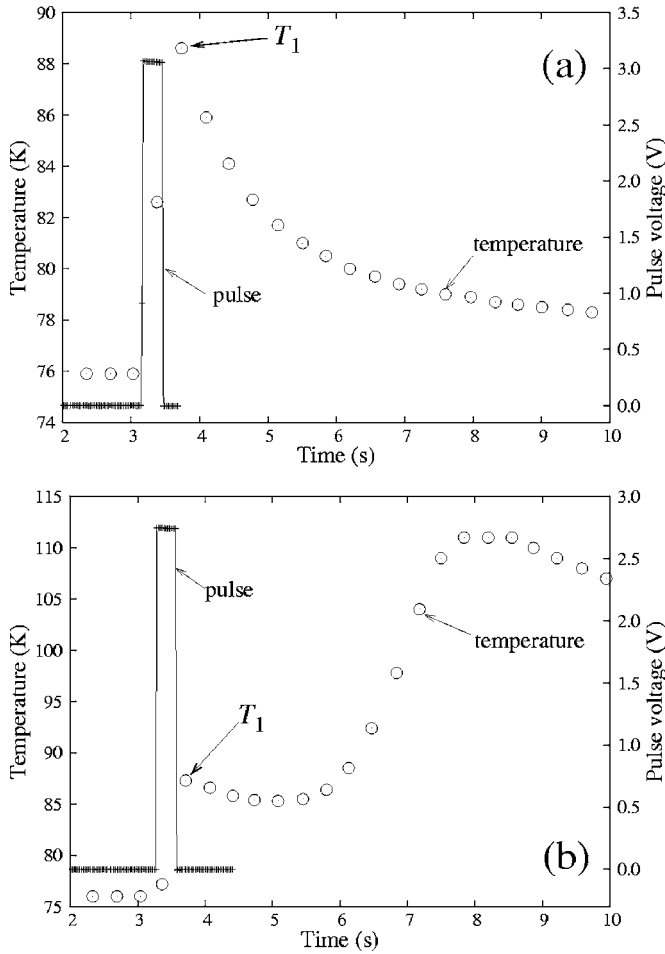


FIG. 9. $T(t)$ in the epoxy measured by the top thermocouple. (a) Without transport current (heater pulse only) and (b) with a transport current and thus subsequent Joule heating. T_1 for Eq. (4) is identified.

$$E_{\text{epo}} = m \int_{T_0}^{T_1} C_{\text{epo}}(T) dT, \quad (4)$$

where m is the epoxy mass, T_0 and T_1 are the initial and final epoxy temperatures during the heat pulse, and $C_{\text{epo}}(T)$ is the epoxy specific heat. It is implicit in Eqs. (2) and (4) that there is no temperature gradient at the heater-tape interface and that the epoxy temperature is uniform. Figure 9(a) gives an example of the epoxy temperature responding to a heat pulse as measured by the thermocouple attached atop the epoxy. In this example, there is no transport current in the sample, so the heater is the only heat source present. The peak temperature T_1 is clearly seen. Figure 9(b) shows the epoxy temperature responding to a heat pulse in a similar case, but with a nonzero transport current in the sample. In this case, T_1 is the first peak in the epoxy temperature that occurs immediately after the heat pulse. Although the transport current results in Joule heating which further heats the epoxy, E_{epo} is the energy into the epoxy from the heat pulse only, so the upper-bound temperature in Eq. (4) is the T_1 illustrated in Fig. 9(b).

The epoxy mass used to attach the heater to the sample ranges from 15 to 20 mg. Using 20 mg in Eq. (4), E_{epo} is

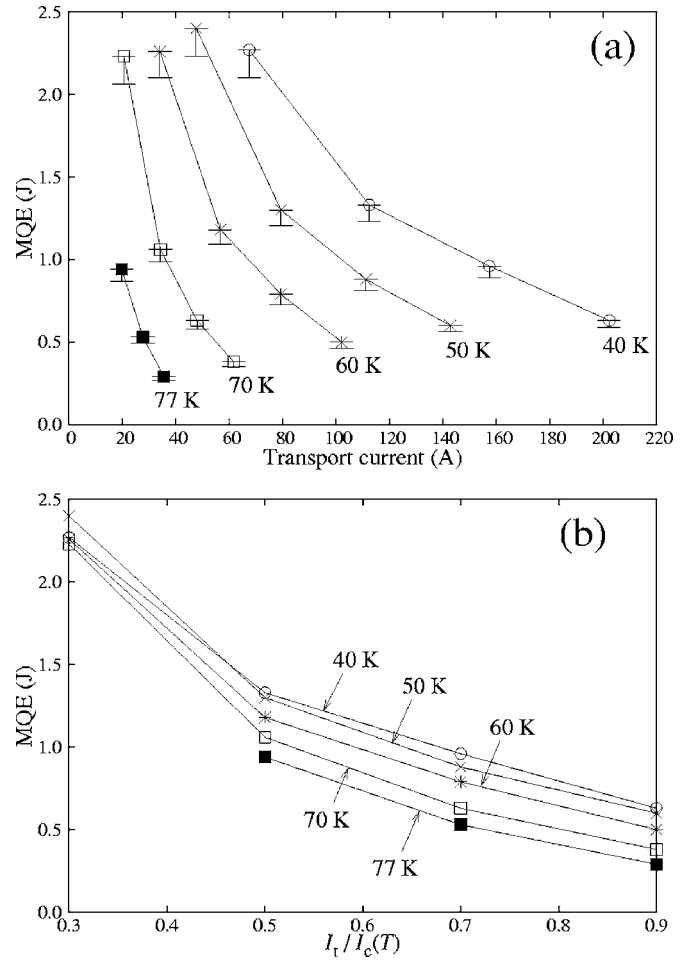


FIG. 10. MQE vs (a) I_t and (b) I_t/I_c measured at 40, 50, 60, 70, and 77 K. The error bars in (a) show the estimated energy absorbed by the epoxy.

calculated and found to be less than 10% of E_{htr} calculated using Eq. (2). The details of $C_{\text{epo}}(T)$ and the E_{epo} values are given in Appendix A.

MQE(I_t, T), as determined using Eq. (1), is plotted in Fig. 10. In Fig. 10(a), the data are plotted as a function of I_t , while in 10(b) the same data are replotted with the transport current normalized by the end-to-end I_c at the individual temperature (I_t/I_c). Note that error bars are also plotted in Fig. 10(a), illustrating the energy absorbed by the epoxy as calculated using Eq. (4). The MQE is on the order of 1 J, ranging from just below 0.5 to 2.5 J. As expected, the MQE increases with decreasing I_t/I_c due to an increased current margin and the resulting reduced Joule heating during current sharing. Note that for the case of $I_t/I_c=0.30$, 77 K, the sample was not quenched for $E_{\text{htr}}=2.68$ J, which was a sufficiently large pulse to destroy the heater. In this case, the $I_t=12$ A, and although a normal zone is initiated by the heat pulse, the Joule heating is very low and cooling from the sample ends prevents a quench. Thus, this configuration is limited at this extreme range of the parameters studied.

C. Normal zone propagation velocity

The NZPV is obtained by dividing the distance between voltage taps (10 mm) by the time delay between the $V(t)$ curves for a fixed reference voltage (V_{ref}), as illustrated in

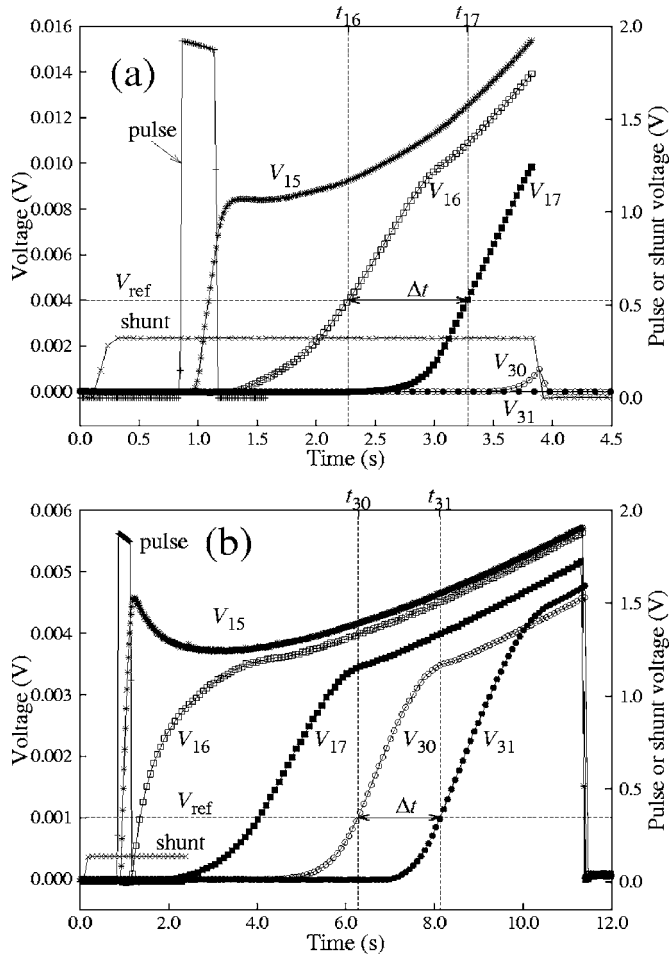


FIG. 11. $V(t)$ for quenches at (a) 50 K, $I_t/I_c=0.50$ and (b) 70 K, $I_t/I_c=0.50$. Also shown are the reference voltages and an illustration of how Δt is calculated for NZPV calculations.

Fig. 11. Two factors that must be addressed are the selection of which voltage taps to use for the calculation and the selection of the V_{ref} .¹²

Ideally, any two neighboring voltage taps will give the same NZPV, but this is not the case because of the experimental conditions. V_{15} is the voltage in the section that contains the heater, so it rises more quickly than the other taps because of the immediate impact of the heat pulse. Thus, using V_{15} will not give a representative value of a steady-state NZPV in a conductor in a magnet. At the conductor ends, V_{11} and V_{32} often do not see a significant voltage because the sample end-to-end voltage limit is reached and the experiment terminated before the quench has propagated sufficiently. Thus, these voltage taps are less useful for determining NZPV. In general, one wants to use sections of the $V(t)$ curves that are parallel; thus, in Fig. 11(a), V_{16} and V_{17} are used. In Fig. 11(b), however, V_{16} appears to be overly influenced by the initial heat pulse (as evidenced by the rapid rise shortly after the heat pulse ended), and either the pair of taps V_{17} and V_{30} , or the pair of taps V_{30} and V_{31} , can be used.

The selection of the V_{ref} is also based on the shapes of the $V(t)$ curves. In general, any V_{ref} within the range of voltages where the chosen $V(t)$ curves are parallel will give the same time difference Δt . For example, in Fig. 11(a), V_{ref} can be anywhere between 1 and 8 mV. In the illustration, V_{ref}

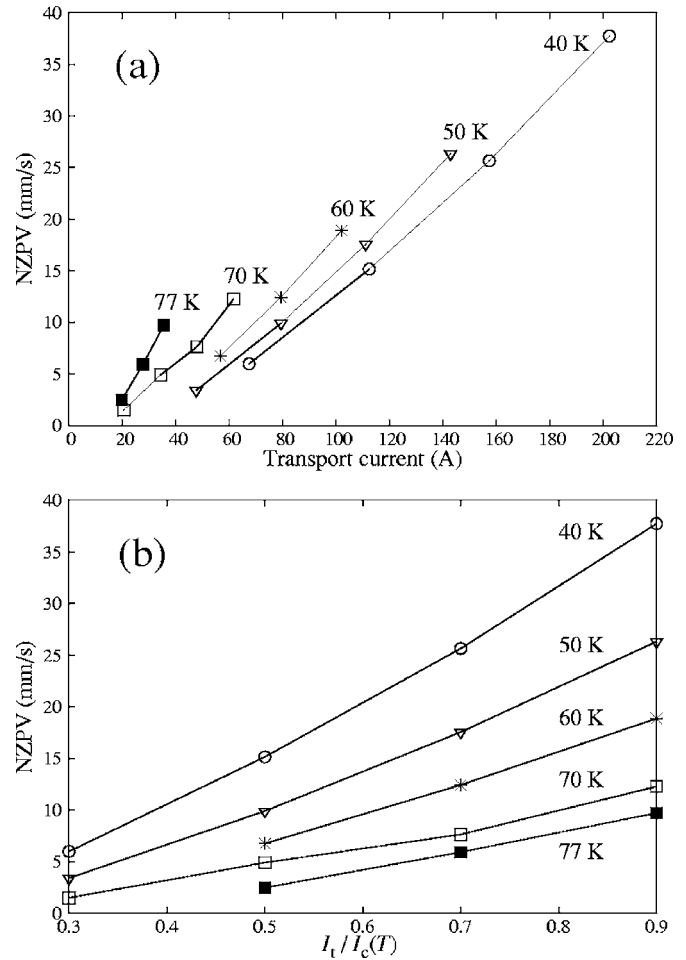


FIG. 12. NZPV vs (a) I_t and (b) I_t/I_c measured at 40, 50, 60, 70, and 77 K.

$=4$ mV is selected and the time difference between $V_{16}=4$ mV and $V_{17}=4$ mV is shown as $\Delta t=t_{17}-t_{16}$. The distance between the voltage taps (10 mm) divided by Δt is then the NZPV for this quench. Comparing Figs. 11(a) and 11(b), one sees that a V_{ref} of 4 mV in Fig. 11(b) would not be appropriate and a lower V_{ref} is required. In this example, a V_{ref} in the range of 0.5–3 mV can be used; $V_{\text{ref}}=1$ mV is selected.

In analyzing these experiments, $V_{16}(t)$ and $V_{17}(t)$ are used for $T < 70$ K with $V_{\text{ref}}=4$ mV, as in Fig. 11(a). For $T=70$ K and $T=77$ K, $V_{16}(t)$ and $V_{17}(t)$ are not parallel [as in Fig. 11(b)], so $V_{30}(t)$ and $V_{31}(t)$ are used with $V_{\text{ref}}=1$ mV. Note that in Fig. 11(b), if $V_{17}(t)$ and $V_{30}(t)$ are used instead, the same NZPV is obtained within 1%. In all cases, if the temporal resolution of the voltage measurements does not provide a measurement at V_{ref} precisely, linear interpolation is used between the measurements just below and above V_{ref} . In this method, the error in Δt is estimated to be 10 ms, which translates into an error in the NZPV of less than 5%.

The NZPV(T, I_t) obtained as described above are shown in Fig. 12. The NZPV range from ~ 1 mm/s to just under 40 mm/s. As I_t and I_t/I_c increase, the NZPV increases and the MQE decreases, indicating that the sample is less stable (see Fig. 10). For example, Fig. 13 plots NZPV and MQE vs I_t/I_c at 40 K. Note that as I_t/I_c varies from 0.30 to 0.90, the NZPV increases by a factor of about 6, while the MQE decreases by almost a factor of 4. This illustrates an intrinsic

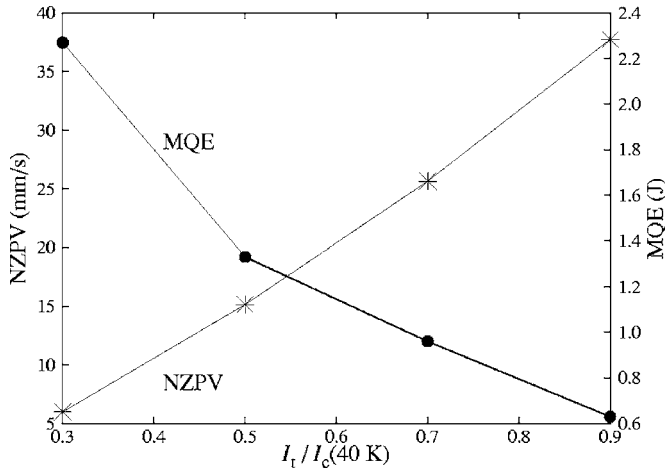


FIG. 13. NZPV and MQE vs I_t/I_c at 40 K. Data are from Figs. 12(b) and 10(b).

trade-off between stability (high MQE) and the requirements for quench detection and protection (high NZPV).

In Fig. 12, the NZPV increases with decreasing temperature, which is related to the temperature dependences of the specific heat and transport current. From Fig. 8(a), $dI_c/dT \sim -4.5$ A/K, so for constant I_t/I_c , I_c increases as T decreases. Specific heat, on the other hand, decreases with T . Thus, for constant I_t/I_c , increasing I_t by decreasing T improves the stability (increases MQE). Using $I_t/I_c=0.70$ as an example, Fig. 14 shows NZPV(T) and MQE(T). As the temperature decreases from 77 to 40 K, I_t increases from 28 to 158 A (565%), NZPV increases from 5.9 to 25.6 mm/s (434%), and the MQE nearly doubles. Thus, reducing T improves conductor performance, stability, and quench behavior simultaneously, indicating that magnets, and large or high energy magnets in particular, should operate at as low a temperature as practical.²² It must still be noted, however, that even though reduced temperature increases the NZPV significantly, it remains two to three orders of magnitude slower than low- T_c magnets at 4.2 K.

The results in Fig. 12 are compared to the classical adiabatic NZPV equation based on constant material properties,²³

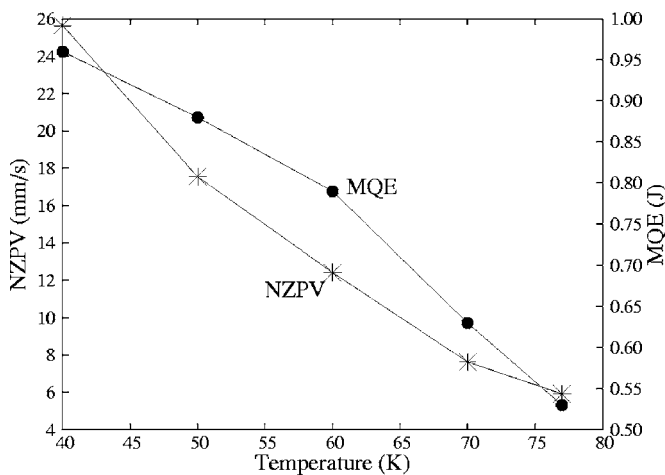


FIG. 14. NZPV and MQE vs T for $I_t/I_c=0.70$. Data are from Figs. 12(b) and 10(b).

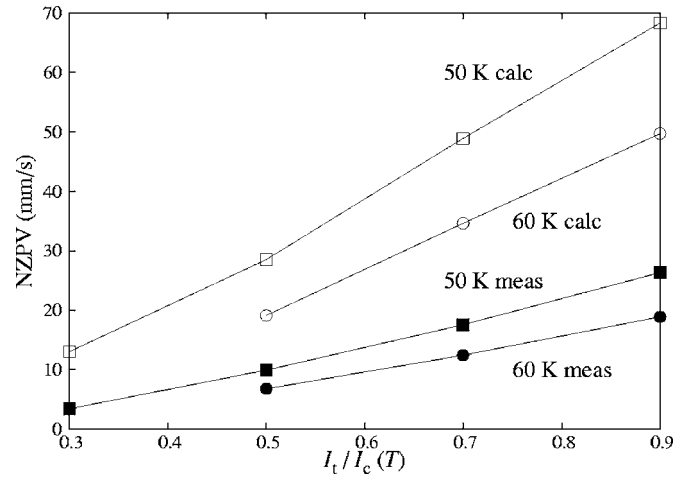


FIG. 15. Comparison of measured and calculated NZPV vs I_t/I_c at 50 and 60 K.

$$\text{NZPV}_{\text{adiabatic}} = \frac{J_m}{C} \sqrt{\frac{\kappa_m \rho_m}{T_t - T_{\text{op}}}}, \quad (5)$$

where J_m is the normal metal current density assuming full current transfer, C the conductor specific heat, κ_m the normal metal thermal conductivity, ρ_m the normal metal resistivity, T_{op} the operating temperature of the conductor, and T_t the transition temperature defined as²³

$$T_t = \frac{T_c + T_{\text{cs}}}{2}, \quad (6)$$

where T_c is the conductor critical temperature and T_{cs} is the current sharing temperature. The current sharing temperature is defined such that $I_t = I_c(T_{\text{cs}})$.²⁴ The Cu and Hastelloy C276 layers dominate the conductor thermal and normal state electrical properties, so the volume-averaged C and κ_m are calculated from these two materials only. Although there is some evidence that some current shares into the Ni-alloy substrate, that current is small and one can assume that the current only shares into the Cu layer. Thus, $\rho_m = \rho_{\text{Cu}}$.²⁵ Sources of material properties are given in Appendix B. To calculate the NZPV using Eq. (5), it is necessary to determine the sample temperature at the same time as $V = V_{\text{ref}}$. ρ_m , κ_m , and C are then determined for that T . For example, in Fig. 11(a), $t_{17} = 3.28$ s when $V_{17} = V_{\text{ref}} = 4$ mV. $T_{17}(t = 3.28$ s) is then obtained from the $T_{17}(t)$ data obtained during the experiment, which in this case is 65 K. Note that this example is an experiment with a starting temperature $T = 50$ K; in this case the neighboring section temperatures are $T_{16}(t = 3.28$ s) = 78 K and $T_{30}(t = 3.28$ s) = 50 K (the normal zone has not yet propagated into this section). Thus, T_{17} is about equal to the average of its adjoining sections and is appropriate to use as a representative of the conductor in this region.

Figure 15 compares the measured and calculated [using Eq. (5)] NZPVs at 50 and 60 K. The calculated velocities are two to three times higher than the measured ones. Possible explanations for the differences are that the temperatures used to determine the material properties are inaccurate, or that heat conduction through the various instrumentation wir-

TABLE I. Sample architectures and geometries used in the comparisons. Here, t is the sample thickness and w is the sample width. Samples 1 and 2 are from Ref. 10 and sample 3 is from Ref. 11.

Sample	t (μm)	w (mm)	Stabilizer [t (μm)]	Substrate [t (μm)]
SPI	180	4	Cu (74)	Hastelloy (100)
1	112	10	Ag (10)	Hastelloy (100)
2	132	10	Ag (30)	Hastelloy (100)
3	129	10	Cu (50)	NiW (75)

ing reduces the NZPV.⁹ More likely, however, is that the material property database is insufficient and thus the values used in the calculation are insufficiently accurate. Furthermore, another significant factor is the interfacial behavior between layers of the conductor.²⁵ The simple model represented by Eq. (5) assumes infinitely fast thermal and electrical diffusion between conductor layers, whereas there is likely to be significant interfacial resistance (thermal and electrical) that slows down the NZPV by increasing the effective ρ_m and κ_m .

D. Comparison with other experimental results

The results reported here are compared with those previously published on YBCO coated conductors tested with a similar¹⁰ or an identical experimental setup.¹¹ The sample architectures and geometries are listed in Table I. Note that the three comparison samples all have a 10 mm width. In general, tape conductors become less stable with increasing width.

It is important to compare the quench behaviors based on I_t/I_c and the minimum quench energy density (MQED), which in this analysis is defined as MQE divided by the conductor cross-sectional area. Figure 16 compares MQED (60 K) of samples 1, 2, and SPI, all having a 100 μm thick Hastelloy substrate. Sample SPI has the highest MQED, which is attributed to the Cu stabilizer and the reduced conductor width.^{26–30} Note that the only difference between samples 1 and 2 is that sample 2 has a 30 μm Ag layer, whereas sample 1 has only a 10 μm Ag layer. Yet, the MQED of sample 2 is much closer to that of sample SPI than it is to that of sample 1. This indicates either that there is a

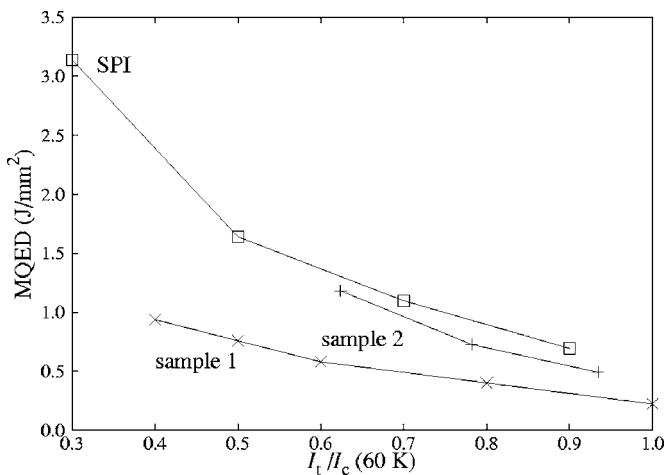


FIG. 16. Comparison of MQED vs I_t/I_c for samples SPI, 1, and 2 at 60 K.

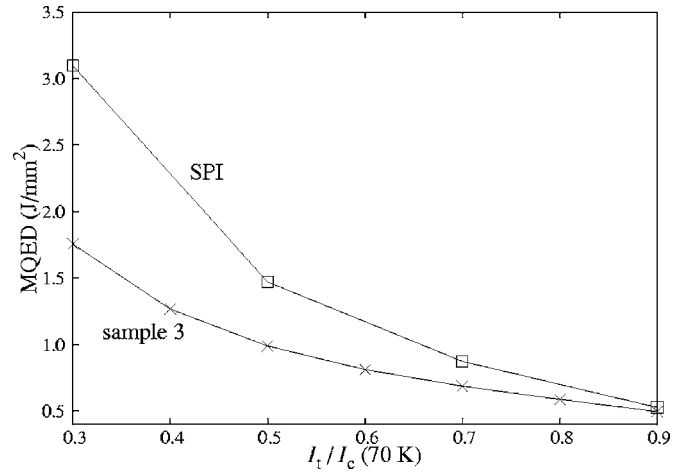


FIG. 17. Comparison of MQED vs I_t/I_c for samples SPI and 3 at 70 K.

substantially diminishing return associated with the increasing stabilizer thickness or that there are other unidentified factors that influence the MQED significantly.

Figure 17 compares MQED (70 K) of samples 3 and SPI. In this case, both conductors have a Cu stabilizer, although it is $\sim 50\%$ thicker for SPI. Sample 3 is grown on a 75 μm NiW substrate and, like samples 1 and 2, is 10 mm wide. SPI is again more stable than the wider conductor, though the difference in MQED (70 K) tends toward zero as I_t/I_c approaches 0.90. This convergence is to be expected; as I_t approaches I_c , MQED approaches zero, remaining nonzero only because of the large thermal mass of the stabilizer and substrate relative to the YBCO layer. The specifics of the conductor architecture (conductor width and relative materials fractions), which play a significant role for most of the parameter range studied, become much less important in the high I_t/I_c limit.

Figure 18 compares the NZPV (70 K) of samples 3 and SPI, showing that NZPV (sample 3) ~ 2 NZPV (SPI). This is consistent with both the higher MQE of SPI and with Eq. (5). At 70 K, the I_c (sample 3) = 205 A and I_c (SPI) = 69 A. Considering only the Cu areas when calculating J_m and assuming that the Cu in each sample has the same residual resistivity ratio (RRR), the relative current densities in the Cu layers are

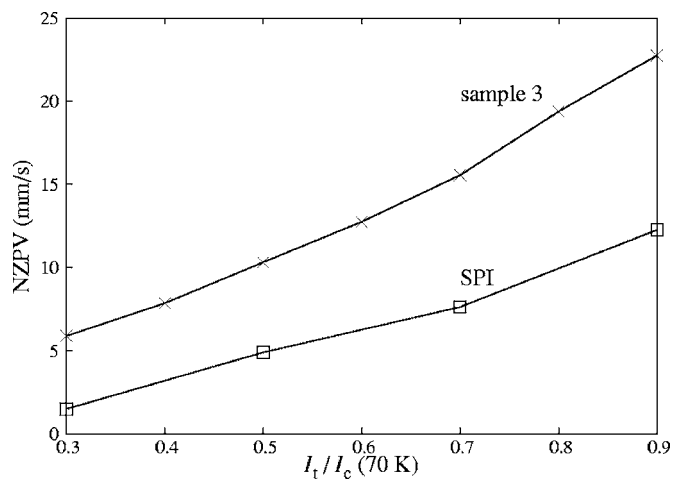


FIG. 18. NZPV vs I_t/I_c at 70 K for samples SPI and 3.

$$J_{m,\text{sample 3}} \sim 2J_{m,\text{SPI}} \quad (7)$$

In Appendix C it is shown that $[1/C\sqrt{\kappa\rho/(T_t-T_{\text{op}})}]_{\text{sample 3}} \approx [1/C\sqrt{\kappa\rho/(T_t-T_{\text{op}})}]_{\text{SPI}}$, so Eqs. (5) and (7) give NZPV (sample 3) ~ 2 NZPV (SPI), consistent with the data in Fig. 18.

IV. CONCLUSIONS

Experimental results are reported on the MQE and NZPV of a 4 mm wide YBCO coated conductor stabilized by Cu on all sides. Measured as a function of temperature and transport current, without a background magnetic field, and in near-adiabatic conditions, the MQE's are on the order of 1 J and the NZPV's range from 1–40 mm/s. These results show that this conductor architecture is more stable than similar architectures that are wider and have less Cu. When comparing the NZPV with the classical adiabatic formula based on volume-averaged material properties, the experimental results are two to three times lower than those calculated. This is attributed to interfacial resistances between layers and uncertainties in the material properties.

For a fixed fraction of I_c , decreasing the operating temperature increases I_t while enhancing both stability and quench propagation. This may push YBCO magnets to operate at lower temperatures, despite the increased cooling costs. Even at lower temperatures, however, the NZPV is orders of magnitude slower than in low- T_c magnets operating at 4.2 K, and innovative approaches to quench detection and protection are required.

ACKNOWLEDGMENTS

We thank Y.-Y. Xie of IGC-SuperPower for providing the coated conductor sample and Y. Iwasa of MIT for the use of a cryocooler. This work was supported by the Air Force Office of Scientific Research and the U.S. Department of Energy through the Center for Advanced Power Systems.

APPENDIX A: ESTIMATED ENERGY ABSORBED BY THE EPOXY

The epoxy specific heat over a wide temperature range is reported in Refs. 31 and 32. The data from Ref. 32 were used here because it covers the temperature range from 2 to 300 K. G3DATA (Ref. 33) was used to read the data points from Fig. 1 in Ref. 31, which were then fit by a sixth order polynomial with GNUPLLOT.³⁴ Equation (4) was then integrated using the sixth order polynomial to determine the values for E_{epo} shown in Table II.

APPENDIX B: MATERIAL PROPERTIES

When estimating the thermal and electrical properties of the Cu layer, RRR=100 was assumed. The Cu specific heat, thermal conductivity, and resistivity are from Refs. 35 and 36. Thermal conductivity data for Hastelloy C276 are available from Ref. 37 for temperatures above 105 K. The thermal conductivity at 20 K is then estimated to be 5 W m⁻¹ K⁻¹ using linear extrapolation. The room temperature resistivity of Hastelloy C276 is 1.3 $\mu\Omega$ m,³⁷ which is

TABLE II. Estimated energy absorbed by the epoxy during the 300 ms heater pulse.

I_t/I_c (%)	T_0 (K)	T_1 (K)	E_{epo} (J)	$E_{\text{epo}}/E_{\text{hr}}$ (%)
90	40	61	0.041	6.6
70	40	71	0.069	7.3
50	40	80	0.099	7.5
30	40	96	0.170	7.5
90	50	67	0.040	6.7
70	50	76	0.068	7.8
50	50	84	0.097	7.5
30	50	100	0.168	7.0
90	60	73	0.036	7.2
70	60	81	0.064	8.2
50	60	87	0.087	7.3
30	60	103	0.161	7.1
90	70	79	0.030	8.0
70	70	85	0.052	8.3
50	70	91	0.077	7.3
30	70	109	0.166	7.4
90	77	83	0.022	7.5
70	77	87	0.038	7.2
50	77	95	0.072	7.7
30	77	120	0.210	7.9

about 78 times higher than that of Cu. The room temperature specific heat of Hastelloy C276 is 427 J kg⁻¹ K⁻¹,³⁷ which is close to that of Ni-based steel listed in Ref. 36 so the data from Ref. 36 are used at all temperatures. The density of Cu is 8960 kg m⁻³ (Ref. 35) and 8890 kg m⁻³ for Hastelloy C276.³⁷

APPENDIX C: NORMAL ZONE PROPAGATION VELOCITY CALCULATION

In this appendix, it is shown that

$$\frac{1}{C_{s3}} \sqrt{\frac{\kappa_{m,s3}\rho_{m,s3}}{T_{t,s3}-T_{\text{op}}}} \approx \frac{1}{C_{\text{SPI}}} \sqrt{\frac{\kappa_{m,\text{SPI}}\rho_{m,\text{SPI}}}{T_{t,\text{SPI}}-T_{\text{op}}}}, \quad (C1)$$

where “s3” stands for “sample 3.” Note that identical temperature-time behavior is assumed for both samples.

Since Cu and Ni-alloy dominate the conductor, the sample specific heat C (J m⁻³ K⁻¹) is estimated using

$$C_{s3} = \frac{t_{\text{Cu},s3}C_{\text{Cu}}d_{\text{Cu}} + t_{\text{NiW}}C_{\text{NiW}}d_{\text{NiW}}}{t_{\text{Cu},s3} + t_{\text{NiW}}}, \quad (C2a)$$

$$C_{\text{SPI}} = \frac{t_{\text{Cu},\text{SPI}}C_{\text{Cu}}d_{\text{Cu}} + t_{\text{Hastelloy}}C_{\text{Hastelloy}}d_{\text{Hastelloy}}}{t_{\text{Cu},\text{SPI}} + t_{\text{Hastelloy}}}, \quad (C2b)$$

where C_{Cu} , C_{NiW} , and $C_{\text{Hastelloy}}$ are in J kg⁻³ K⁻¹, d is the density in kg m⁻³, and the thicknesses are $t_{\text{Cu}}=50$ μm , $t_{\text{NiW}}=75$ μm , $t_{\text{Cu},\text{SPI}}=74$ μm , and $t_{\text{Hastelloy}}=100$ μm . The density of NiW alloy is assumed to be the same as that of Hastelloy. The specific heat of Cu is very close to that of Ni-alloy. Using numerical values of C_{Cu} and $C_{\text{Ni-alloy}}$, $C_{s3} \sim C_{\text{SPI}}$ is found (see Table III).

TABLE III. Comparison of the specific heats of Cu and Ni-alloy and the ratio of conductor specific heats for samples 3 and SPI.

T (K)	C_{Cu} ($\text{J kg}^{-1} \text{K}^{-1}$)	$C_{\text{Ni-alloy}}$ ($\text{J kg}^{-1} \text{K}^{-1}$)	$C_{\text{sample 3}}/C_{\text{SPI}}$
60	135	93	0.990
70	170	128	0.993
80	205	167	0.995
90	230	203	0.997
100	251	234	0.998

The thermal conductivity κ_m is obtained using the rule of mixtures (volume averaging) of Cu and the substrate, κ_{Cu} and κ_{sub} , as given by

$$\kappa_{s3} = \frac{t_{\text{Cu},s3}\kappa_{\text{Cu}} + t_{\text{NiW}}\kappa_{\text{NiW}}}{t_{\text{Cu},s3} + t_{\text{NiW}}}, \quad (\text{C3a})$$

$$\kappa_{\text{SPI}} = \frac{t_{\text{Cu,SPI}}\kappa_{\text{Cu}} + t_{\text{Hastelloy}}\kappa_{\text{Hastelloy}}}{t_{\text{Cu,SPI}} + t_{\text{Hastelloy}}}. \quad (\text{C3b})$$

For $T=70$ K, $\kappa_{\text{Cu}} \sim 600 \text{ W m}^{-1} \text{K}^{-1}$ (Ref. 35) and $\kappa_{\text{Hastelloy}}$ and κ_{NiW} are less than or close to $10 \text{ W m}^{-1} \text{K}^{-1}$.^{37,38} So the contribution from the Ni-alloy is neglected and Eq. (C3) becomes

$$\kappa_{s3} \approx \frac{50\kappa_{\text{Cu}}}{50 + 75} = 0.4\kappa_{\text{Cu}}, \quad (\text{C4a})$$

$$\kappa_{\text{SPI}} \approx \frac{74\kappa_{\text{Cu}}}{74 + 100} = 0.425\kappa_{\text{Cu}}. \quad (\text{C4b})$$

Thus, $\kappa_{s3} \approx \kappa_{\text{SPI}}$.

Assuming that the current shares into the Cu only, the matrix resistivities become $\rho_{m,s3} = \rho_{m,\text{SPI}} = \rho_{\text{Cu}}$. $I_c(T)$ for samples 3 and SPI are fit to linear functions using GNUPLOT,

$$I_{c,s3} = -12.0201 \times T + 1052.42, \quad (\text{C5a})$$

$$I_{c,\text{SPI}} = -4.41332 \times T + 378.806. \quad (\text{C5b})$$

Dividing both sides of Eq. (C5a) by 3 shows that $I_{c,s3}(T) \sim 3I_{c,\text{SPI}}(T)$ for all temperatures. Thus, for fixed I_t/I_c , the current sharing temperatures are equal.²⁴ As the $T_{c,s3} \approx T_{c,\text{SPI}}$ (within 2 K), $T_{t,s3} \approx T_{t,\text{SPI}}$.

Combining Eqs. (C2)–(C5), it is seen that for fixed T_{op} , Eq. (C1) is true.

¹C. E. Oberly, G. Kozlowski, and R. J. Fingers, Adv. Cryog. Eng. **38B**, 479 (1992).

²Y. Iwasa, Cryogenics **43**, 303 (2003).

³Y. Iwasa, Physica C **426–431**, 1348 (2005).

⁴Y. Iwasa, IEEE Trans. Appl. Supercond. **15**, 1615 (2005).

⁵D. Larbalestier, A. Gurevich, D. M. Feldmann, and A. Polyanskii, Nature (London) **414**, 368 (2001).

⁶R. C. Duckworth, Ph.D. thesis, University of Wisconsin-Madison, 2001.

⁷R. C. Duckworth, J. M. Pfothenhauer, J. W. Lue, M. J. Gouge, D. F. Lee, and D. M. Kroeger, Adv. Cryog. Eng. **48**, 313 (2002).

⁸J. W. Lue, M. J. Gouge, R. C. Duckworth, D. F. Lee, D. M. Kroeger, and J. M. Pfothenhauer, Adv. Cryog. Eng. **48**, 321 (2002).

⁹R. Grabovickic, J. W. Lue, M. J. Gouge, J. A. Demko, and R. C. Duckworth, IEEE Trans. Appl. Supercond. **13**, 1726 (2003).

¹⁰A. Ishiyama, M. Yanai, T. Morisaki, H. Ueda, Y. Shiohara, T. Izumi, Y. Iijima, and T. Saitoh, IEEE Trans. Appl. Supercond. **15**, 1659 (2005).

¹¹X. Wang, A. R. Caruso, M. Breschi, G. Zhang, U. P. Trociewitz, H. W. Weijers, and J. Schwartz, IEEE Trans. Appl. Supercond. **15**, 2586 (2005).

¹²F. Trillaud, H. Palanki, U. P. Trociewitz, S. H. Thompson, H. W. Weijers, and J. Schwartz, Cryogenics **43**, 271 (2003).

¹³Y. Iwasa, H. Lee, J. Fang, and B. Haid, IEEE Trans. Appl. Supercond. **13**, 1772 (2003).

¹⁴H. M. Kim, J. Jankowski, H. Lee, J. Bascuñán, S. Fleshler, and Y. Iwasa, IEEE Trans. Appl. Supercond. **14**, 1290 (2004).

¹⁵Y. Iwasa *et al.*, IEEE Trans. Appl. Supercond. **15**, 1683 (2005).

¹⁶M. Dixit, T. Kim, H. Kim, K. J. Song, S. S. Oh, R. K. Ko, H. S. Kim, and K. B. Park, Physica C **434**, 199 (2006).

¹⁷P. N. Barnes and M. D. Sumption, J. Appl. Phys. **96**, 6550 (2004).

¹⁸A. Mbaruku, U. P. Trociewitz, X. Wang, and J. Schwartz, IEEE Trans. Appl. Supercond. (in press).

¹⁹M. N. Wilson, *Superconducting Magnets* (Oxford University Press, New York, 1983), Chap. 9, p. 207.

²⁰F. Trillaud, F. Ayela, A. Devred, M. Fratini, D. Leboeuf, and P. Tixador, IEEE Trans. Appl. Supercond. **15**, 3648 (2005).

²¹V. Selvamanickam *et al.*, IEEE Trans. Appl. Supercond. **15**, 2596 (2005).

²²C. E. Oberly, presented at the CHATS Applied Superconductivity Workshop 2006, Lawrence Berkeley National Laboratory ([http://supercon.lbl.gov/chats/Talks/Wednesday morning/CEOberly.ppt](http://supercon.lbl.gov/chats/Talks/Wednesday%20morning/CEOberly.ppt)).

²³Y. Iwasa, *Case Studies in Superconducting Magnets*, 1st ed. (Plenum, New York, 1994), Chap. 4, pp. 347–350.

²⁴L. Dresner, *Stability of Superconductors* (Plenum, New York, 1995), Chap. 3, pp. 36–37.

²⁵M. Breschi, P. L. Ribani, X. Wang, and J. Schwartz, Supercond. Sci. Technol. (submitted).

²⁶H. R. Hart, Jr., Proceedings of the 1968 Summer Study on Superconducting Devices and Accelerators, 1968 (unpublished), pt. 11, pp. 571–600, BNL Report No. 50155 (C-551) (<http://www.bnl.gov/magnets/Staff/Gupta/Summer1968/0571.pdf>).

²⁷J. Schwartz, J. P. Freidberg, and J. E. C. Williams, Cryogenics **31**, 21 (1991).

²⁸J. Schwartz, J. P. Freidberg, and J. E. C. Williams, IEEE Trans. Magn. **27**, 2120 (1991).

²⁹E. E. Burkhardt, S. Nakamae, and J. Schwartz, IEEE Trans. Appl. Supercond. **5**, 393 (1995).

³⁰E. E. Burkhardt and J. Schwartz, IEEE Trans. Appl. Supercond. **9**, 240 (1999).

³¹C. Swenson, Rev. Sci. Instrum. **68**, 1312 (1997), **68**, 2596(E) (1997).

³²P. Javorský, F. Wastin, E. Colineau, J. Rebizant, P. Boulet, and G. Stewart, J. Nucl. Mater. **344**, 50 (2005).

³³J. Frantz, G3DATA, Version 1.50 (<http://www.frantz.fi/software/g3data.php>).

³⁴Gnuplot development team, GNUPLOT Version 4.0 (<http://www.gnuplot.info/>).

³⁵CRYOCOMP, properties version 3.06, Eckels Engineering Inc.

³⁶Cryogenic technologies group at National Institute of Standards and Technology, Material Properties (http://cryogenics.nist.gov/NewFiles/material_properties.html).

³⁷Haynes International, Inc., Hastelloy C-276 alloy product brochure (<http://www.haynesintl.com/mini/C276s/C276.htm>).

³⁸C. L. H. Thieme, D. Aized, and O. A. Chevtchenko, presentation 3MC08 given at the Applied Superconductivity Conference, Seattle, Washington, August 30, 2006.